Diagnosis of Rotor Asymmetries in Induction Motors: A Steady State Approach Using Rotating Frame References

Francisco Vedreño Santos, Lucia Frosini, and Daniel Moriñigo Sotelo

Abstract-- The diagnostic of electrical machines is of paramount importance, particularly with the Motor Current Signature Analysis (MCSA) method. MCSA stands out as a potent and non-intrusive tool for evaluating the condition of electric motors. This paper introduces an innovative approach for the diagnosis of rotor asymmetries, broken rotor bars, in induction machines operating in steady state directly fed from the grid, emphasising the decomposition of line currents within specific rotating frames. A novel methodology is proposed, and its results are meticulously compared with those obtained through the conventional Fast Fourier Transform (FFT) diagnostic technique. In particular, the newly introduced methodology exhibits enhanced sensitivity, surpassing the capabilities of conventional FFT. Additionally, the innovative approach is proven to be capable of quantifying the increase in fault harmonics in correlation with the load on the machine, aligning with the results observed through conventional FFT analysis. The findings strongly indicate that this pioneering technique offers a more robust and reliable means of diagnosing induction machines when compared to the traditional FFT method, by enhancing sensitivity and providing a nuanced understanding of fault harmonic variations with load changes.

Keywords—broken rotor bars, fault diagnosis, induction machines, motor current signature analysis, MCSA, rotor asymmetry, rotating frame, signal processing, steady state,

1 Introduction

Induction machines are the workhorse of industry and are well-known for their reliability and durability. However, they are still susceptible to failure. Rotor cage faults occur in percentages ranging from 7% to 12% of total induction motor failures [1]-[3]. Despite their relatively low rate of occurrence, detecting and diagnosing these faults is vital due to their potential to trigger severe side effects. Broken rotor fragments can hit the stator winding, inflicting serious damage to its insulation. Furthermore, the redistribution of currents in adjacent bars rises thermal stress, leading to a gradual propagation of the fault, underlining the critical role of diagnostics in pre-empting such complications.

As reviewed in [4], the main cause of rotor cage failures lies in weak connections between the cage bars and its end rings that are worsened by operating conditions that induce overheating and thermal stress. The probability of a rotor cage failure is greatly related to the rotor manufacturing process. Fabricated rotors are more susceptible to rotor cage faults, as they tend to appear as a breakage of a rotor bar near the weld between the bar and the short-circuit end ring. In contrast, die-cast rotors have greater resilience to this failure and rarely suffer from it. A particular case is given by submersible motors for deep wells: these motors have fabricated copper bars, but instead of an end ring made up of a solid piece, they use multiple copper foils with the same shape as ferromagnetic laminations. This type of end ring is prone to accelerated wear due to internal cooling water and high-speed rotation [5]. Additionally, manufacturing flaws, such as material impurities, presence of porosity (air bubbles), magnetic anisotropy of the laminations, or imperfections, contribute to deficiencies in the rotor cage.

In the long term, these factors become more pronounced, particularly under magnetic stresses induced by magnetic forces, variable frequency content or additional harmonics (leading to magnetic saturation effects), local maxima of magnetic fields at sharp edges and corners, and irregular distribution of eddy currents [6]. Environmental factors, such as humidity, dust, high pressure, and corrosive agents [4]-[7], also play a significant role in the deterioration of the rotor cages leading to an asymmetric rotor.

The asymmetry resulting from the breakage of the rotor bars disrupts the distribution of the magnetic flux. Rotor flux perceives this disruption as an open or partially open circuit, especially if the bar is cracked rather than completely broken [8]. These distorted rotor flux contribute to the generation of unaccounted electromagnetic torque, leading to increased torque and

This work was supported in part by the Universidad de Valladolid (Spain).

F. Vedreño Santos is with School of Computing Engineering and the Built Environment, Edinburgh Napier University, Edinburgh EH10 5DT, United Kingdom (e-mail: f.vedrenosantos@napier.ac.uk)

L. Frosini is with Department of Electrical, Computer and Biomedical Engineering, University of Pavia, 27100 Pavia, Italy (e-mail: lucia.frosini@unipv.it)

D. Moriñigo Sotelo is with the Research Group ADIRE-HSPDigital, ITAP Institute, Universidad de Valladolid, 47009 Valladolid, Spain (e-mail: daniel.morinigo@uva.es)

speed ripple. As a result, higher levels of noise and vibration are produced within the motor. Furthermore, bar breakages can also affect the laminations close to the points where they occur.

In summary, a defect in the rotor cage of an induction motor produces a distortion in the magnetic flux of the rotor. As torque production is primarily based on the interaction between the magnetic fluxes of the stator and the rotor, which are connected to each other by slip and, therefore, by speed, any irregularities in the rotor flux cause ripples in the stator flux. These fluctuations are then transmitted to the stator current, as explained in [9],[10], and manifest themselves as additional harmonics in the currents.

Numerous diagnostic techniques have been developed for steady-state diagnosis of broken bars in induction motors. Among all the techniques developed, FFT emerged as the most prevalent of all [11]-[18], [23]-[25], [27]-[30]. Reference [11] shows the conventional use of the FFT for the diagnosis of broken bars in induction machines, while [12] and [13] are two recent good reviews of diagnostic techniques for rotor asymmetries. Additionally, [14] is a good review that focuses on intelligent techniques for fault diagnosis of rotating machinery.

It is worth commenting that, recently, alternative methods, such as integrating stray flux measurements with FFT or Short-Time Fourier Transform (STFT) analysis, have been proposed [15], [16]. In [17], Independent Component Analysis (ICA) was employed to process FFT spectra for fault detection, supported by Artificial Neural Networks (ANN), while [18] utilised FFT spectra within an intelligent multi-agent system to detect broken rotor bars.

Deep learning approaches techniques have also been developed for rotor asymmetries in induction motors. [19] extends the use of Convolutional Neural Network (CNN) and Recursive Neural Network (RNN) by incorporating Natural Language Processing (NLP) to enhance previous learning models for the diagnosis of induction motors. In [20] machine learning techniques such as Random Forest (RF), ANN, k-Nearest Neighbors (kNN), and Decision Tree (DT), are evaluated using a confusing matrix for the diagnosis of rotor asymmetries in induction motors, concluding that RF outperforms the other models evaluated. Finally, [21] employs the Principal Component Analysis (PCA) and PLECS-Matlab co-simulations to train a model for fault detection in induction machines using ratio of variances and the Hotelling's T^2 distribution.

The use of four different complex filters based on the Kalman filter for the diagnosis of Wound Rotor Induction Motors (WRIM) is presented in [22]. The variations of these complex filters are the Dual Unscented Kalman Filter (DUKF), the Extended Kalman Filter (EKF), the Dual Extended Kalman Filter (DEKF) and Unscented Kalman Filter (UKF) concluding that the DUKF is the best option among the four.

In off-line testing, [23] introduced an enhanced Discrete Fourier Transform (DFT) with zero-padding of the sampled stator current to mitigate FFT spectral leakage for broken bar diagnosis. References [24] and [25] applied FFT to the stator current in the d-q frame, leveraging the robustness of this approach in distinguishing broken bars from mechanical oscillations. While [24] utilized the magnitude of certain frequency components in active and reactive current spectra as fault indicators, [25] demonstrated the immunity of the d-component of current to load oscillations, proposing its spectrum as a fault indicator. In particular, [24] required three-phase current measurements. In [26] the normalised frequency domain energy operator, combined with complex operators such as the Teager-Kaiser energy operator, are employed to diagnose rotor asymmetries under steady and slightly varying speed conditions.

Park's vector approach [27]-[33] has also been utilised to identify rotor asymmetry faults in induction motors effectively. These references are relevant to this work, as they also focus on decomposing currents either in fixed frames or within the frequency supply frame. For example, in [27], fault detection relies on scrutinizing the deformation of Park's currents to discern potential motor faults. In [28], a departure from conventional Park's vector analysis is noted, where active and reactive current Park's vectors are employed to detect rotor asymmetries under load oscillations. Meanwhile, [29] explores the diagnosis of faults, examining the Hilbert Modulus Current Space Vector (HMCSV) and the Hilbert Phase Current Space Vector (HPCSV) through the FFT. The findings suggest that the HPCSV spectrum exhibits a richer harmonic content compared to that of the HMCSV spectrum. In [30] introduces a method involving the application of elliptic and notch filters on Park's vector components, followed by monitoring the higher harmonic index.

More recent advances in the fault diagnosis techniques by using the Park's vector approach are [31]-[33]. In [31] the MCSA and the Extended Park's vector approach utilising both neural and non-neural methods are developed. This study explores the PCA, Curvilinear Component Analysis (CCA) and Independent Component Analysis (ICA), alongside linear dimensional reduction techniques such as Long Short-Term Memory (LSTM) and Shallow Dense Neural Networks (SDNN), concluding that the PCA-SDNN achieves the best accuracy. In [32] a comparison between the Model Based Residual Spectrum Analysis (MRSA) with the conventional extended Park's vector Modulus approach is carried out, showing that the MRSA exhibits superior sensitivity and performance for the diagnosis of rotor asymmetries in induction motors. Finally [33] applies the DWT to analyse the stator phase current and the Energy Eigen Value (EEV) analysis to determine the severity of faults in rotor asymmetries. This study finds that the methodology performs better when the control of the machine is done by the Predictive Torque Control (PTC) rather than when the control is done by the Direct Torque Control (DTC).

One of the common denominators of the diagnostic techniques already developed is that they are based on sophisticated signal processing techniques, intricate filters, and artificial intelligence methods. However, these methods are typically computationally intensive. While these approaches have proven effective in the detection of rotor asymmetries, they come with

several inherent limitations.

Firstly, these methods are typically computationally intensive, requiring significant processing power and specialised hardware, which may not be feasible low-cost industrial settings. The complexity of these techniques also demands extensive data preprocessing and parameter tuning, which can introduce variability in diagnostic accuracy and reliability.

Secondly, many of these approaches depend on large datasets for training and validation, particularly in the case of machine learning and deep learning-based methods. The availability of high-quality data is often limited, and the process of acquiring such data can be time-consuming and costly. Moreover, AI-driven techniques may struggle when generalising as they may require retraining or fine-tuning when applied to different machines or operating conditions.

Additionally, some traditional signal processing methods, such as wavelet analysis or empirical mode decomposition, require expert knowledge for proper implementation and interpretation of the results. The effectiveness of these methods is highly dependent on the selection of appropriate parameters, such as decomposition levels, filter bandwidths, mother wavelet functions, etc, which can vary across different applications.

Another critical limitation can be their sensitivity to noise and environmental disturbance as many industrial environments are subjected to them. While advanced filtering techniques can mitigate some of these effects, they often add another layer of complexity and computational burden.

Finally, the integration of these techniques into existing monitoring systems can be challenging due to the need of specialised software or hardware increasing the overall cost of implementation, in contrast to the more efficient and computationally lightweight approach developed in this work.

This research introduces an innovative methodology that avoids complex signal processing or filtering, centred on calculating the average value of stator currents decomposed in a rotating frame, reducing the complexity of the approach and its computational effort for the diagnosis of rotor asymmetries in induction machines fed directly from the grid. The main contributions of this study are:

- Introduction of a new harmonic-aligned rotating frame approach for the diagnosis of rotor asymmetries in induction motors.
- Enhanced sensitivity of the rotor asymmetry fault detection compared to conventional FFT approaches.
- Ability to quantify the fault severity based on the load by using normalised values.
- Reduction of the computational complexity compared to the conventional FFT approaches by tracking harmonics in steady state conditions.
- Validation of the results with experimental data comparing healthy versus faulty squirrel cage induction motors with different levels of load.

The paper is structured as follows: Section 2 presents the physical basis of broken bar faults, while Section 3 introduces the novel methodology for diagnosis within rotating frames. Section 4 details the proposed approach, followed by the experimental validation in Section 5, where the results are compared with conventional FFT techniques. Finally, Section 6 offers the conclusions and highlights the main findings of this study.

2 Physical Basis Fault

Rotor asymmetries in induction machines are a phenomenon associated with actual faults, such as Broken Rotor Bars (BRB). These faults cause asymmetries between phase impedances that lead to unbalanced phase currents. Consequently, a negative sequence system of currents flows through the windings, producing inverse rotating magnetic fields. These inverse magnetic fields induce the characteristic harmonic components in the currents of the windings installed at the other side of the air gap.

This paper introduces a methodology based on the well-established Motor Current Signal Analysis (MSCA) theory for the detection of characteristic patterns of the fault components produced by rotor asymmetries.

A rotor asymmetry produces a substantial increase in the amplitude of the lower and upper sideband components of the stator current, whose frequencies are given by [34]:

$$f_{ra}(s) = (1 \pm 2 \cdot s) \cdot f_{sup} \tag{1}$$

where f_{ra} are the frequencies of the main rotor asymmetry fault-related components in the stator current in Hz, s is the slip at which the induction motor is operating per unit, and f_{sup} is the supply frequency in Hz.

Conventional MCSA uses (1) to find the frequencies at the current spectrum, where the fault components appear when a rotor asymmetry fault is developed.

3 Physical Basis Approach

The distribution of currents along the periphery of an electrical machine's stator is a crucial factor in determining its magnetic field as the current sheet [35] represents the density of current per unit of peripheral length in the air gap, essentially denoting the linear current density of the load within the machine.

However, in practical scenarios, the current sheet within real machines is a discrete function due to the presence of individual

conductors housed within the machine's slots. This discrete nature is not ideal for mathematical analysis. To overcome this, the current sheet is expanded into a Fourier series. This transformation results in a set of spatial current sheets, all exhibiting sinusoidal characteristics and corresponding to different harmonics.

The most common scenario in industrial settings involves three-phase symmetrical machines, where the real axis, x, is oriented to align with the direction and magnitude of the R phase (Fig. 1). In a machine featuring three independent phases, where the currents $i_R(t)$, $i_S(t)$ and $i_T(t)$ flow through its winding, regardless of the number of pole pairs, p, the machine's current sheet is expressed as:

$$i_{rst,h}(t) = i_R(t) + i_S(t) \cdot e^{jh\gamma} + i_T(t) \cdot e^{j2h\gamma} \tag{2}$$

where $\gamma = 2 \cdot \pi/3$ and h is the harmonic order.

In an ideal scenario under a constant load, a current sheet would adhere to a precise path, represented by a dashed line in Fig. 1, indicating a uniform and consistent current distribution in the air gap without any presence of harmonics. However, when harmonics are introduced into the system, they disrupt this uniformity, causing the current sheet to undergo modulation. This modulation manifests as oscillations between the inner and outer solid black circles drawn in Fig. 1.

The introduction of harmonics denotes the incorporation of additional frequencies beyond the fundamental supply frequency. These additional frequencies alter the pure sinusoidal waveform of the current, leading to fluctuations or variations in its behaviour. The observed oscillations between the inner and outer solid black circles signify the resultant changes in the amplitude or spatial distribution of the current sheet due to the presence of these harmonic frequencies or changes in load.

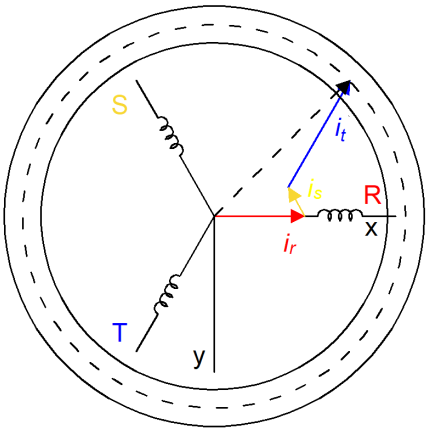

Fig. 1. Generic current sheet in an induction machine stator

The resultant current sheet, depicted by the black dashed vector in Fig. 1, combines all the current harmonics inherent in the line currents. This current sheet can be mathematically represented through a Fourier series as follows:

$$i(t) = i_0 + \sum_{n=1}^{n=\infty} i_n \cdot \sin(\omega_n \cdot t + \varphi_n) \tag{3}$$

This equation shows the decomposition of the current sheet into a series comprising a DC value in amperes, i_0, and an infinite sum of harmonic components, $\sum_{n=1}^{n=\infty} i_n \cdot \sin(\omega_n \cdot t + \varphi_n)$, where i_n is the n-harmonic magnitude in amperes, ω_n is the n- harmonic angular frequency in rad/s, t is the time in seconds and φ_n is the initial shift angle in radians of each harmonic component.

The representation of the current sheet, the black dashed vector, based on its harmonic components, is illustrated in Fig. 2. It is important to note that, for simplicity, the depiction in Fig. 2 involves only two harmonics at constant load, represented by solid blue and red vectors, chosen without sacrificing the generality of the concept. This simplified representation aids in visualizing the impact of harmonics on the overall nature of the current sheet: as if there were no harmonics, the current sheet will rotate following the dashed circle, or the trajectory of the blue vector, whereas the introduction of harmonics, the red vector, modulates the current sheet between the solid black inner and outer circles.

The current sheet represented by the black dashed line in Fig. 2 can be projected onto either the x or y fixed axis displayed in it. However, this decomposition into a fixed frame does not offer significant benefits because projecting the current sheet onto either axis yields a modulated waveform similar to the original current sheet. Hence, such projection does not distinctly simplify the current analysis.

When comparing the use of the current sheet versus employing the FFT methods that rely on a single-line current analysis, the advantage lies in potentially reducing specific harmonics. For instance, the current sheet might diminish certain harmonics, such as the third or multiples of three, in comparison to a single-line current.

This paper proposes a novel approach centred on establishing a rotating frame precisely aligned with the harmonic of interest to track it effectively. This innovative approach involves synchronising a rotating frame to the desired harmonic frequency. By aligning a rotating frame precisely with the desired harmonic and allowing it to rotate at the harmonic frequency, the projection of this harmonic onto the x_{r1} rotating frame remains constant, as depicted in Fig. 3. Simultaneously, the average value of other harmonics on the rotating frame becomes zero due to their sinusoidal nature. Moreover, when projected onto the y_{r1} axis of the rotating frame, the tracked harmonic also registers an average value of zero.

This innovative approach of employing a rotating frame aligned with specific harmonics aims to provide a clearer and more stable representation of the desired harmonic, facilitating its isolation and analysis by effectively nullifying other harmonic components that might introduce noise or unwanted variations into the analysis. This pioneering technique not only enhances the precision of isolating and analysing specific harmonics but also offers a structured and reliable methodology for fault detection and diagnosis, leveraging the advantages of a rotating frame aligned with the targeted harmonic of interest.

4 Proposed Approach

The proposed approach for harmonic tracking of machine currents in their rotating frame involves a systematic series of steps, which are:

1. Decompose the voltages in a fixed frame.
2. Calculate the instantaneous frequency of the voltage phasor.
3. Decompose the line currents in a fixed frame.
4. Determine the frequency of the harmonics to track.
5. Find the initial shift angle of the rotating frame that rotates at the fundamental harmonic frequency.
6. Find the initial shift angle of the rotating frame which rotates at the fault harmonic frequency.
7. Determine the current of the fundamental harmonic aligned with the x_{r1} rotating at the speed of the fundamental current, $I_{xr1fsup}$.
8. Determine the current of the fault harmonic aligned with the x_{r1} rotating at the speed of the fault current, I_{xr1fra}.
9. Normalise and quantify the severity of the fault.

A flowchart showing the nine steps involved in doing the proposed approach is presented in Fig. 4

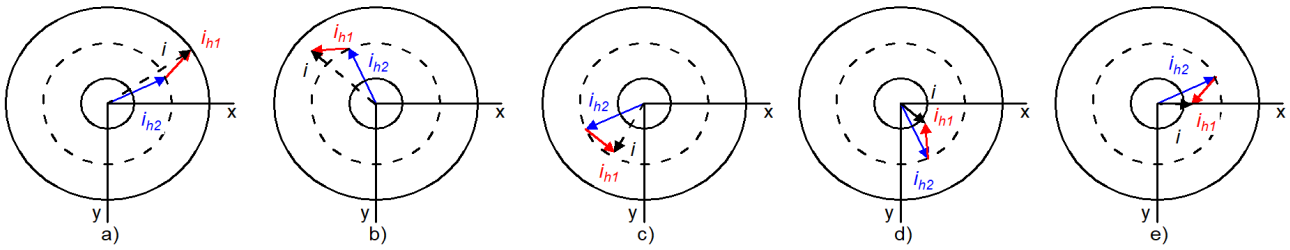

Fig. 2. Modulation of the current sheet due to harmonics on a fixed reference frame, *x*-*y*. The blue harmonic has a frequency f_r and a magnitude *m*, and the red harmonic has a frequency 1.5 x f_r and a magnitude 0.5 x *m*. a) Initial, b) Initial position + 72 electrical degrees, c) Initial position + 144 electrical degrees, d) Initial position + 216 electrical degrees, e) Initial position + 360 electrical degrees

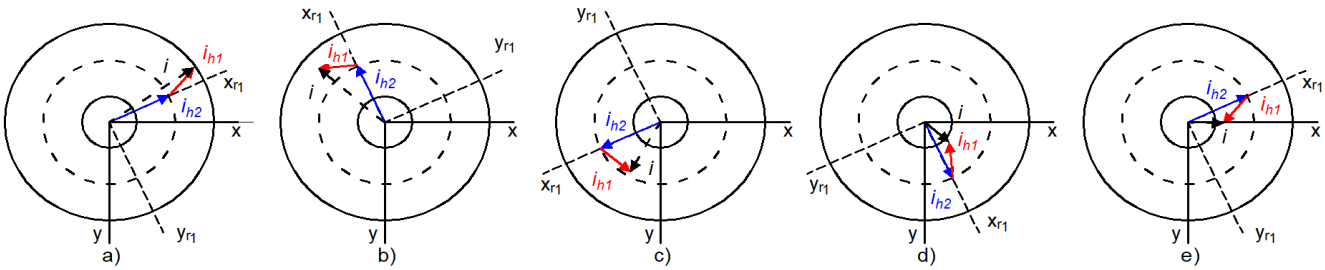

Fig. 3. Representation of the current sheet harmonics on a rotating frame at a frequency f_r , x_{r1}-y_{r1}, where the x-axis is aligned with the blue harmonic. The blue harmonic has a frequency f_r and a magnitude *m*, and the red harmonic has a frequency 1.5 x f_r and a magnitude 0.5 x *m*. a) Initial, b) Initial position + 72 electrical degrees, c) Initial position + 144 electrical degrees, d) Initial position + 216 electrical degrees, e) Initial position + 360 electrical degrees

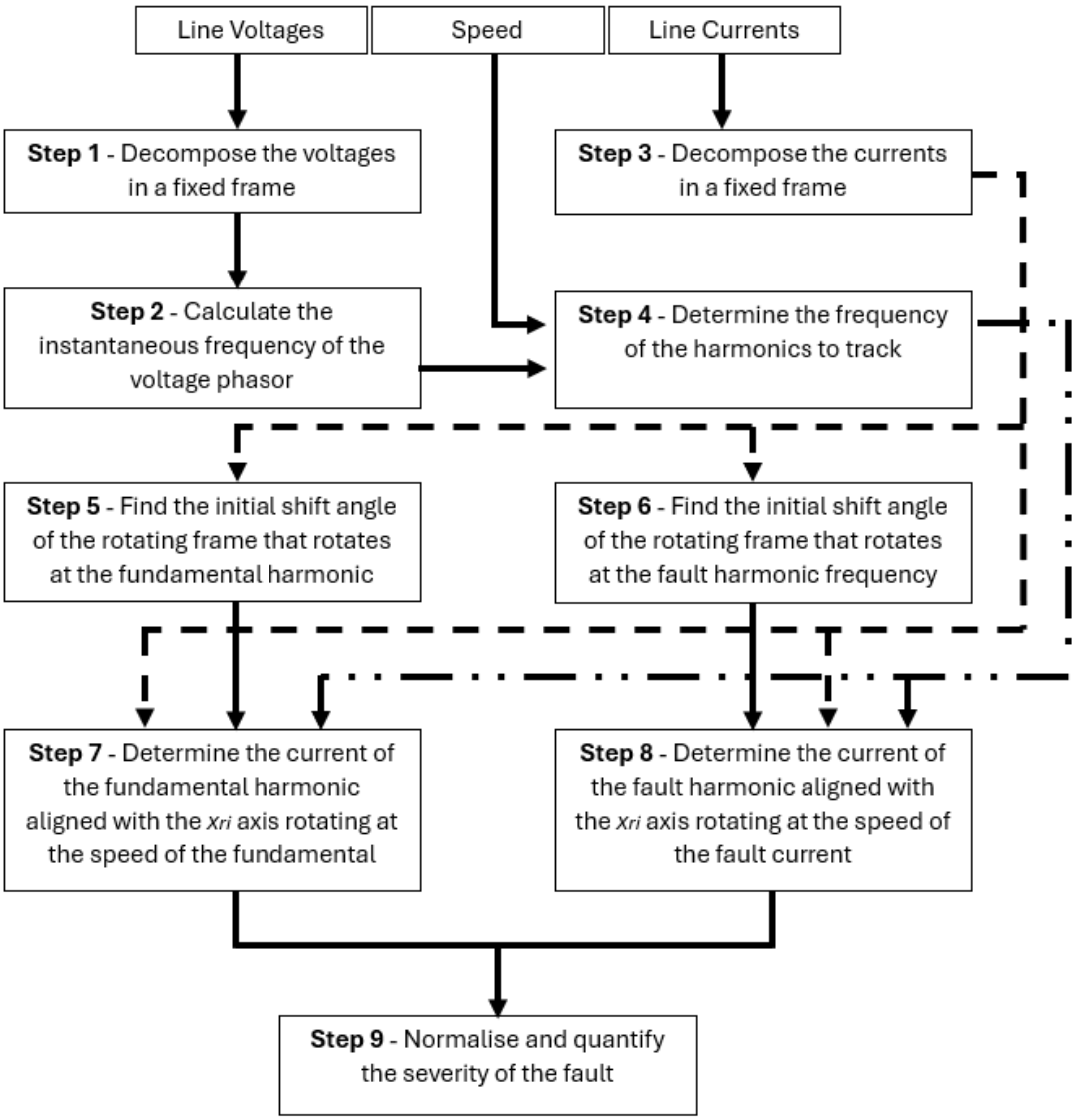

Fig. 4. Flow chart of the implementation of the proposed approach

The actual implementation of the proposed approach is as follows. Initially, the voltages, $v_R(t)$, $v_S(t)$ and $v_T(t)$ are decomposed into a fixed reference frame, *x*-*y*, through (4) and (5), where $v_x(t)$ is the projection of the current sheet on the x-axis and $v_y(t)$ on the y-axis:

$$v_x(t) = \frac{2}{3} \cdot v_R(t) - \frac{1}{3} \cdot v_S(t) - \frac{1}{3} \cdot v_T(t) \tag{4}$$

$$v_y(t) = -\frac{1}{\sqrt{3}} \cdot v_S(t) + \frac{1}{\sqrt{3}} \cdot v_T(t) \tag{5}$$

Once that is done, the next step is to find the angle of the voltage, which will allow the calculation of the instantaneous frequency of the fundamental harmonic. The angle of the phasor voltage can be found by:

$$v_{angle}(t) = \tan^{-1}\left(\frac{v_y(t)}{v_x(t)}\right) \tag{6}$$

And the instantaneous frequency of the supply is calculated as:

$$f_{sup}(t) = \frac{dv_{angle}(t)}{dt} \tag{7}$$

The currents, $i_R(t)$, $i_S(t)$ and $i_T(t)$, are also decomposed into the same fixed frame, where the voltages where previously decomposed, using (8) and (9), where $i_x(t)$ is the projection of the current sheet on the *x*-axis and $i_y(t)$ on the *y*-axis of the fixed reference frame:

$$i_x(t) = \frac{2}{3} \cdot i_R(t) - \frac{1}{3} \cdot i_S(t) - \frac{1}{3} \cdot i_T(t) \tag{8}$$

$$i_y(t) = -\frac{1}{\sqrt{3}} \cdot i_S(t) + \frac{1}{\sqrt{3}} \cdot i_T(t) \tag{9}$$

Subsequently, the components $i_x(t)$ and $i_y(t)$ projected on the fixed reference frame are projected now into the rotating fundamental frequency reference frame, which axes are x_{rlfsup} and y_{rlfsup}, and on the fault harmonic frequencies reference frame, which axes are x_{rlfra} and y_{rlfra}, computed by using (10) and (11).

$$i_{xr1_h}(t) = i_x(t) \cdot \cos\left(\omega_{frame_h} \cdot \mathrm{t} + \varphi_{0_\mathrm{h}}\right) - i_y(t) \cdot \sin\left(\omega_{frame_h} \cdot \mathrm{t} + \varphi_{0_\mathrm{h}}\right) \tag{10}$$

$$i_{yr1_h}(t) = i_x(t) \cdot \sin\left(\omega_{frame_h} \cdot \mathrm{t} + \varphi_{0_\mathrm{h}}\right) + + i_y(t) \cdot \cos\left(\omega_{frame_h} \cdot \mathrm{t} + \varphi_{0_\mathrm{h}}\right) \tag{11}$$

The decomposition of the harmonic of interest involves knowing the angular rotational frequency of the desired harmonic, ω_{frame_h}, and the initial shift angle, φ_{0_h}, of the rotating frame.

For the fundamental frequency, ω_{frame_h} is set as:

$$\omega_{frame_h} = \omega_{frame_{fsup}} = 2 \cdot \pi \cdot f_{sup} \tag{12}$$

It is also necessary to find the value of $\varphi_{0_{fsup}}$ which is equal to φ_{0_h}, (11), when the condition $i_{yr1_h} = 0$, (11), with $\omega_{frame_h} = \omega_{frame_{fsup}}$, is satisfied.

The fault harmonic, ω_{frame_h}, which is related to the mechanical speed, is calculated through (13):

$$\omega_{frame_h} = \omega_{frame_{fra}} = 2 \cdot \pi \cdot f_{ra} \tag{13}$$

Analogously as for the fundamental frequency, $\varphi_{0_{fra}}$ is equal to φ_{0_h}, (11), when the condition $i_{yr1_h} = 0$, (11), with $\omega_{frame_h} = \omega_{frame_{fra}}$ is satisfied.

A more detailed explanation of the decomposition of voltage and current vectors in fixed and rotating frames can be found in [36]. Following the determination of the rotating frame speed, ω_{frame_h} and initial shift angle φ_{0_h} for each harmonic from (11), the $i_{xr1_h}(t)$ component is recalculated by inputting the now known ω_{frame_h} and φ_{0_h} values into (10).

Finally, these recalculated values are normalised and transformed into a logarithmic scale using (14), which calculates the Power Spectrum Density (PSD), the measure of the signal's power content versus its frequencies, of the analysed signals:

$$\mathrm{PSD} = 20 \cdot \log_{10}\left(\left|\frac{\overline{i_{xr1\,fra}}}{\overline{i_{xr1\,fsup}}}\right|\right) \tag{14}$$

where $\overline{i_{xr1\,fra}}$ represents the average value of current sheet in the fault harmonic rotating frame, and $\overline{i_{xr1\,fsup}}$ represents the average of the current in the fundamental frequency component. This comprehensive approach enables the quantification and normalization of the fault in the system.

5 Experimental Validation

5.1 Experimental Setup

The experimental setup, Fig. 5, comprises two Siemens 750 W squirrel cage induction motors (1LA7083-4AA10) with the following rated values: 230/400 V, 3.2/1.6 A Δ/Y, 1395 rpm, $\cos(\varphi) = 0.81$, 50 Hz. They are arranged in a star configuration and connected to the power grid. The load for these motors is provided by a Lucas Nülle magnetic-powder brake, along with its corresponding control unit, enabling precise measurement of torque and speed signals.

The data collection is carried out by two custom-made boards, each equipped with voltage and current Hall-effect transducers manufactured by LEM. The data acquisition system uses a National Instruments (NI) cDAQ 9174 chassis equipped with NI 9215 modules.

One of the induction motors underwent a modification to emulate the BRB fault condition under investigation, whereas the other remained unmodified. Specifically, in the faulty motor, a hole was strategically drilled in the squirrel cage end ring at a rotor bar end, mitigating potential damage to the rotor lamination as shown in Fig. 6.

Two Load Levels (LL), 50% and 70% of the rated values of the induction motors, were selected to test the proposed methodology. These specific load levels were chosen as induction motors are designed to operate efficiently within the 50% to 100% range of its rated load, with a peak efficiency typically occurring around 75% of the rated load [37]. Additionally, induction motors are commonly operated below their full rated load to provide spare capacity for potential overloads.

Diagnosing BRB at load levels lower than the rated load is known to present additional challenges. At lower load levels than the rated load point, the magnitudes of the BRB fault harmonics are reduced, and the fault harmonics are closer to the fundamental frequency, making their detection more challenging than at the machine's rated load. Therefore, testing induction motors at 50% and 70% load levels is considered to provide a practical and relevant assessment of the proposed methodology, reflecting common industrial operating conditions.

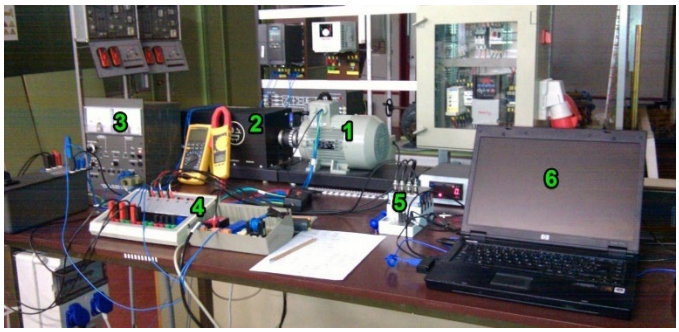

Fig. 5. Test bench: (1) Induction motor under test; (2) Magnetic powder brake; (3) Control unit; (4) Bespoken board with Hall effect transducers for current and voltage measurements; (5) DAQ board by National Instruments; (6) Laptop.

Fig. 6. Squirrel cage induction machine rotor with a broken bar.

For each load level, 10 tests were conducted, 5 on a healthy motor and 5 on a motor with a broken bar. This dual load approach ensures a comprehensive evaluation of the proposed diagnostic technique's performance across different operational conditions, providing a well-rounded perspective on its behaviour and response under different load levels. During each test, the three-phase currents, voltages, and motor speed were recorded with a sampling frequency of 50 kHz for a duration of 10 seconds.

Subsequently, the 20 tests were analysed using a MATLAB script where the proposed approach was implemented, as detailed in section 4. The analysis was performed on MATLAB version R2023b, running on a Windows 11 laptop equipped with a 12th generation Intel® Core™ i7-1255U processor (1.70 GHz), a 64-bit operating system, and 32 GB of RAM. The results of this analysis are presented in the following subsection.

5.2 Results

The experimental results are organised into three tables. Table 1 shows the supply frequency at which both motors are fed from the grid and the fault harmonic frequency function of the speed for each test performed at the two different load levels.

Table 2 provides the initial shift angles of the supply and fault harmonic rotating frames, which are a crucial step in the harmonic tracking. The shift angle values in Table 2 ensure the correct alignment of the rotating frames for both the supply and fault harmonics. The correct alignment is fundamental for the accurate harmonic decomposition and subsequent fault analysis.

Table 3 shows a comprehensive quantification of the fault analysis. Table 3 compares the PSD values considering both healthy and faulty states and load levels. The quantification of the proposed methodology aligns with the conventional results obtained via FFT analysis of the *R* phase current. This comparison offers a validation and a broader perspective on the fault assessment methodology employed. The experimental process is explained in detail in the following paragraphs.

Table 1. Supply frequency, f_{sup}, and fault frequency, f_{ra}, of the tests.

Test Load	Test	f_{sup} (Hz)		f_{ra} (Hz)	
		Healthy	BRB	Healthy	BRB
Load Level 1 50% of the rated load	1	50.06	50.00	47.19	47.19
	2	50.01	50.00	47.07	47.27
	3	50.01	50.04	47.06	47.22
	4	50.00	50.04	47.02	47.25
	5	50.01	50.02	47.07	47.31
Load Level 2 70% of the rated load	1	50.01	50.01	45.71	45.39
	2	50.01	50.03	45.76	45.50
	3	50.00	50.00	45.57	45.25
	4	50.01	49.99	45.50	45.26
	5	49.98	49.98	45.55	45.35

Table 2. Initial shift angle of the supply, $\varphi_{0_{fsup}}$, and fault, $\varphi_{0_{ffra}}$, rotating frames.

Test Load	Test	Initial shift angle, $\varphi_{0_{fsup}}$, of the fundamental harmonic rotating frame (°)		Initial shift angle, $\varphi_{0_{ffra}}$, of the fault harmonic rotating frame (°)	
		Healthy	BRB	Healthy	BRB
Load Level 1 50% of the rated load	1	90.3	56.3	33.3	99.3
	2	167.7	172.7	21.1	69.2
	3	35.6	155.6	20.4	93.2
	4	16.4	11.6	84.1	43.0
	5	113.3	63.5	157.4	6.0
Load Level 2 70% of the rated load	1	15.2	18.1	178.4	117.2
	2	2.2	56.9	18.7	121.3
	3	100.5	27.6	158.8	43.7
	4	138.8	71.4	121.9	153.6
	5	114.8	163.1	4.0	32.9

Table 3. Quantification of the fault by the new proposed method and the conventional FFT method.

Test Load	Test	Proposed method PSD (dBs)			FFT PSD (dBs)		
		Healthy	BRB	ΔPSD	Healthy	BRB	ΔPSD
Load Level 1 50% of the rated load	1	-85.27	-57.40	27.87	-66.73	-56.34	10.39
	2	-89.60	-57.49	32.11	-66.54	-57.38	9.16
	3	-84.23	-56.62	27.61	-71.55	-56.05	15.50
	4	-90.24	-60.00	30.24	-68.93	-55.80	13.13
	5	-87.91	-57.70	30.21	-68.98	-56.87	12.11
Load Level 2 70% of the rated load	1	-94.29	-60.42	33.87	-72.42	-53.46	18.96
	2	-108.11	-63.26	44.85	-71.53	-53.63	17.90
	3	-87.99	-58.25	29.74	-68.99	-54.19	14.80
	4	-90.37	-60.22	30.15	-71.01	-53.28	17.73
	5	-98.39	-54.50	43.89	-69.37	-54.40	14.97

The practical diagnosis process starts by recording the speed, which allows the calculation of the fault frequency component, three-phase voltages, which allow the calculation of the grid frequency, and three-phase currents, which allow the calculation of the current sheet, as shown in Fig. 7 to Fig. 9 for the particular load level of 50% of the rated load of the machine under investigation.

The three voltages are transformed into the *x-y* fixed axis using (4) and (5) to determine the supply frequency. The resulting *x-y* representation of the voltages is shown in Fig. 10. The instantaneous angle and frequency of the supply are then calculated using (6) and (7).

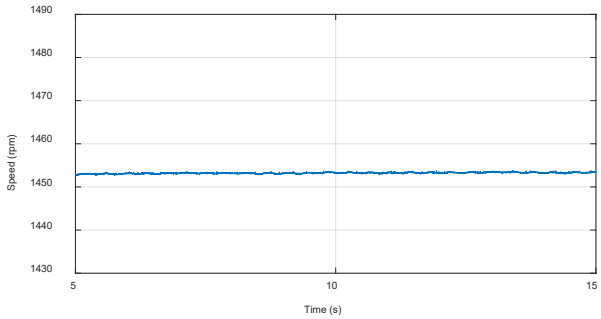

a)

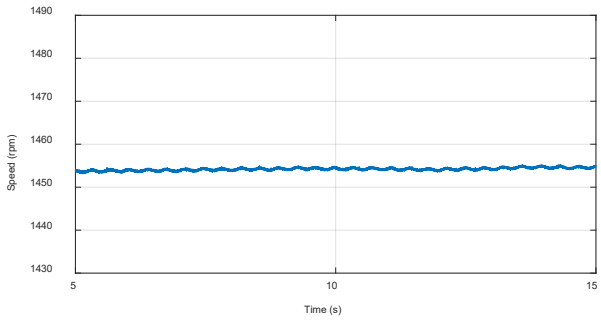

b)

Fig. 7. Steady state speed for the induction motor under test with one broken bar at 50% of the rated load. a) Healthy, b) Faulty

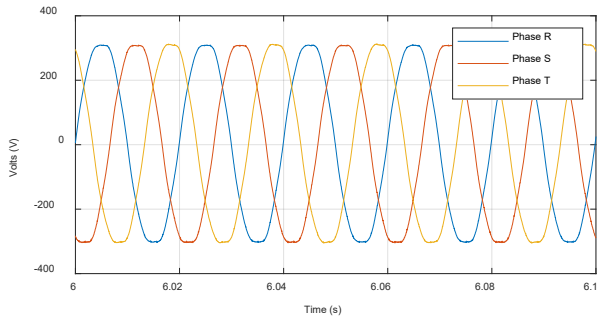

a)

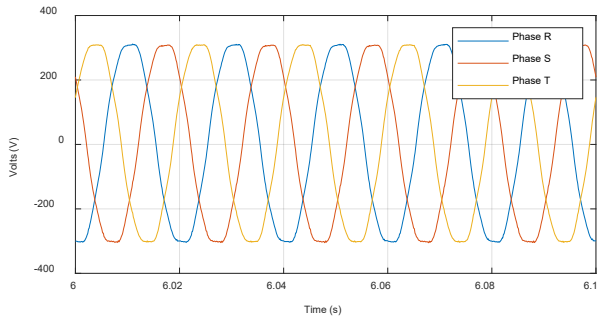

b)

Fig. 8. Three phase voltages supplied to the stator of the induction motors under test with one broken bar. Phase R in blue colour, phase S in red colour and phase T in orange colour, at 50% of the rated load of the machine under investigation. a) Healthy, b) Faulty

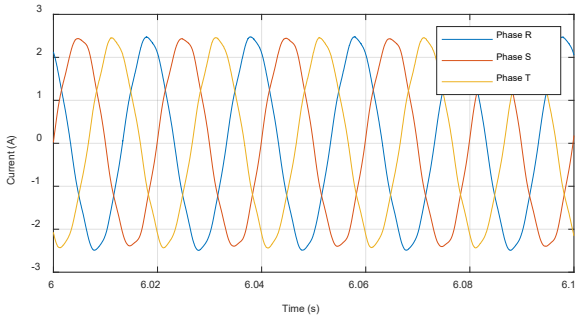

a)

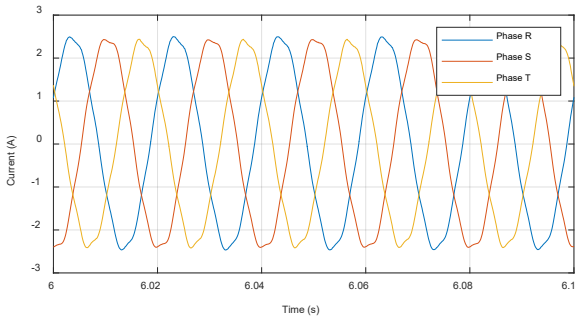

b)

Fig. 9. Three phase currents from the stator of the induction motors under test with one broken bar. Phase R in blue colour, phase S in red colour and phase T in orange colour, at 50% of the rated load of the machine under investigation. a) Healthy, b) Faulty

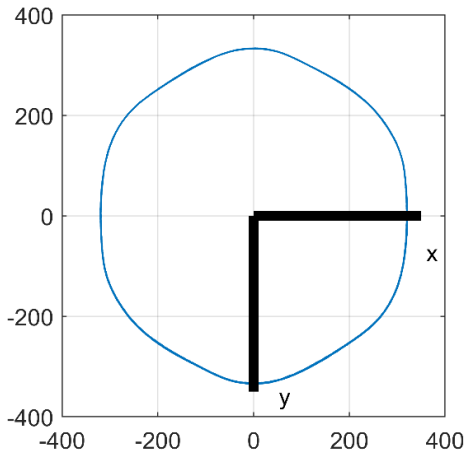

Fig. 10. Decomposition of the three phase voltages on the fixed *x*-*y* axis.

The next step is to decompose the currents on the fixed *x*-*y* axis using (8) and (9), enabling their further decomposition in the supply and fault frequency rotating frames through (10) and (11). To achieve a correct decomposition into the rotating frames, the frequency and initial shift angle of the rotating frame must be known. The rotating frame speed is derived using (12) and (13), respectively, from the supply and fault frequencies reported in Table 1. The initial shift angle for the supply frequency rotating frame, $\varphi_{0_{fsup}}$, is then determined by an iterative algorithm which aligns the x_{rl} axis of the rotating frame at the supply frequency with the harmonic rotating at the supply frequency of the current. This process is repeated for the fault frequency rotating frame, where the fault frequency rotating frame is aligned with the harmonic rotating at the fault frequency, returning the initial shift angle for the fault frequency rotating frame, $\varphi_{0_{fra}}$. All the initial shift angles, $\varphi_{0_{fsup}}$ and $\varphi_{0_{fra}}$, for each test are shown in Table 2.

Upon correct alignment of the rotating frames, the current is decomposed onto the supply frequency rotating frame in its x_{rlfsup} component using (10). The x_{rlfsup} component becomes a DC signal with high-frequency ripple due to inherent harmonics in the currents, as depicted in Fig. 11. The value of interest is the average value of the x_{rlfsup} component, denoted as $\overline{i_{xr1\ fsup}}$, as other harmonic components average to zero due to their sinusoidal nature.

This process is replicated for the rotating frame set at the fault component frequency. The current phasor representation in

this frame yields a sinusoidal current at the frequency difference between the supply and fault component frequencies, as shown in Fig. 12. As for the supply frequency rotating frame, the interest lies in the average value of the x_{r1fra} component, denoted as $\overline{\iota_{xr1\,fra}}$, representing the fault harmonic magnitude, as other harmonic components average to zero due to their sinusoidal nature.

Finally, the DC components of the phasor current rotating at the supply and fault frequencies, shown in Fig. 11 and Fig. 12, are inputted into (14) to determine the machine's state. The quantification of the fault is presented in Table 3 and compared to the results obtained via conventional FFT analysis of the *R* phase current, satisfactorily validating the newly employed fault assessment methodology.

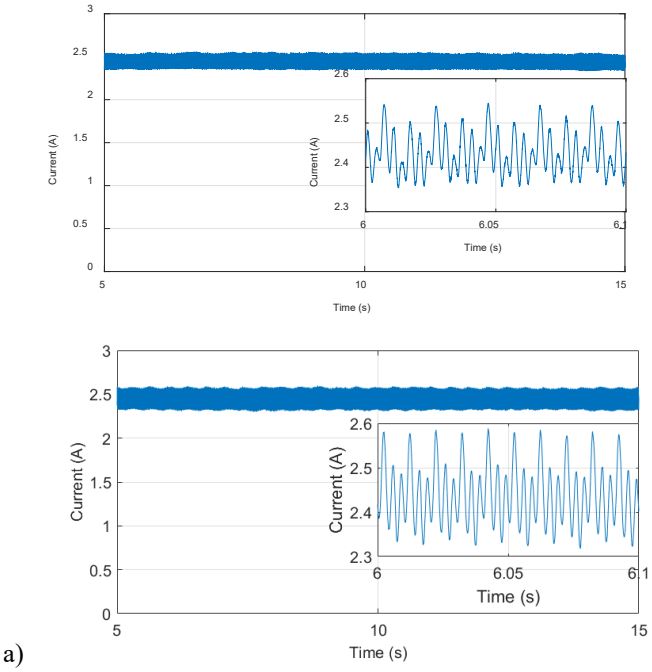

Fig. 11. Representation of the three phase currents on the rotating frame at the supply frequency fully aligned with the x_{r1} axis at 50% load. a) Healthy, b) Faulty

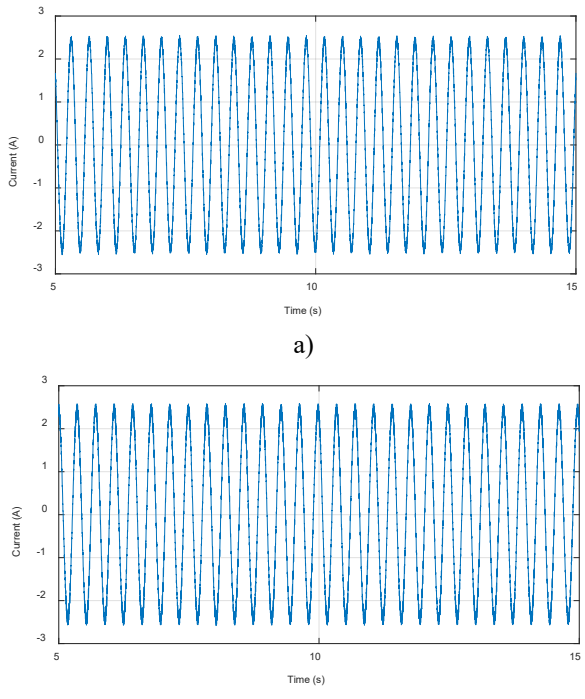

Fig. 12. Representation of the three phase currents on the rotating frame at the fault frequency fully aligned with the x_{r1} axis at 50% load. a) Healthy, b) Faulty

Table 3 highlights a substantial distinction in the quantification of healthy and faulty states when employing the proposed method. Specifically, the difference between a healthy and faulty state, (15), as determined by this method, is consistently at least 27 dBs greater than that observed when the machine is analysed using conventional FFT analysis. In contrast, the conventional FFT diagnostic technique demonstrates a discernible but comparatively smaller difference of at least 9 dBs between healthy and faulty states.

$$\Delta PSD = PSD_{BRB} - PSD_{Healthy} \tag{15}$$

Furthermore, the new proposed method is also able to quantify the severity of the fault function of the load of the machine: as it is seen in Table 3, the fault quantification difference tends to increase when the machine is more loaded following a similar trend that is seen when the machine is diagnosed by the conventional FFT technique.

The proposed methodology shows a greater distinction between healthy and faulty states than the conventional FFT and robustness across different load conditions. From Table 3 it is seen that the quantification difference between the faulty and healthy states tends to increase with higher machine loads. This suggests that the proposed method is sensitive to fault progression and can capture subtle variations in the currents that become more pronounced as the load increases.

Under lower load conditions, the method still provides a clear distinction between healthy and faulty states with greater sensitivity than the conventional FFT. As the load increases, the PSD difference grows even larger, indicating that the method effectively captures the intensification of the fault related signature. This behaviour aligns with the physical expectation that rotor asymmetries generate stronger harmonic distortions when the motor operates under higher torque demands.

6 Conclusions

This paper introduced an innovative methodology for diagnosing induction machines operating in steady state, focusing on the decomposition of the fundamental and fault frequency components in rotating frames. The proposed methodology is systematically compared to the conventional FFT diagnostic technique, revealing comparable results with an additional noteworthy advantage as the new methodology demonstrates increased sensitivity in contrast to the conventional FFT technique. Specifically, the conventional FFT technique exhibits a difference of approximately 10 dB between a healthy machine and a faulty machine. The newly proposed methodology yields a substantial difference of around 30 dB, underscoring its superior sensitivity in distinguishing between healthy and faulty machine states.

Furthermore, the new methodology can also quantify the severity of faults in relation to the load on the machine. The observed increase in the difference between healthy and faulty cases with an increase in machine load aligns with the trends seen in the conventional FFT technique, indicating that the proposed methodology effectively captures the severity of the fault in a manner consistent with established diagnostic approaches.

This new methodology can be applied to the diagnosis of rotor asymmetries, and it can potentially be extended to other faults such as eccentricity (static, dynamic, or mixed) or bearings. The main drawback of this new method is its inability to diagnose rotor asymmetries under transient conditions. Since this approach relies on a numerical diagnosis rather than the interpretation of graphical results, and its calculations align with those used in vector control of induction machines, it appears to be a strong candidate for integration into Variable Speed Drives (VSD) for automatic fault detection in induction motors. Both the drawback of the approach and its practical implementation in VSD are potential future research works.

These compelling findings emphasise the enhanced sensitivity and efficacy of the newly introduced fault assessment methodology. The results suggest that this innovative approach offers a more robust and reliable means of diagnosing machine states compared to traditional FFT analysis, marking a significant advancement in the field of induction machine diagnostics.

7 Appendix

Table 4 summarises the nomenclature employed in the paper by showing the symbols, their definitions and their units to enhance the readability of the work.

Table 4. Nomenclature

Symbol	Definition	Units	Symbol	Definition	Units
f_{ra}	Frequencies of the main rotor asymmetry fault-related components in the stator current	Hz	$i_{xr1h}(t)$	Projection of the current phasor on the *x*-axis of rotating frame of frequency *h*	A
f_{sup}	Supply frequency	Hz	$i_{yr1h}(t)$	Projection of the current phasor on the *y*-axis of rotating frame of frequency *h*	A
γ	Constant equal to $2 \cdot \pi/3$	rad	p	Pole pairs	
h	Harmonic order		φ_n	Initial shift angle of the *n*-harmonic	rad
$i(t)$	Total current sheet	A	φ_{0h}	Initial shift angle of a phasor at frequency *h*	rad
i_0	DC current	A	s	Slip	PU
$i_{hi}(t)$	Current phasor of harmonic *i*	A	t	Time	s
i_n	*n*-harmonic magnitude	A	$v_{angle}(t)$	Angle of the voltage phasor	rad
$i_R(t)$	Line current phase R	A	$v_R(t)$	Line voltage phase R	V
$i_{rst,h}(t)$	Current sheet of harmonic order *h*	A	$v_S(t)$	Line voltage phase S	V
$i_S(t)$	Line current phase S	A	$v_T(t)$	Line voltage phase T	V
$i_T(t)$	Line current phase T	A	$v_x(t)$	Projection of the voltage phasor on fixed *x*-axis	V
$i_x(t)$	Projection of the current phasor on the *x*-axis of a fixed frame	A	$v_y(t)$	Projection of the voltage phasor on fixed *y*-axis	V
$i_y(t)$	Projection of the current phasor on the *y*-axis of a fixed frame	A	ω_{frameh}	Angular frequency of a rotating frame at frequency *h*	rad/s
$i_{xr1fra}(t)$	Current phasor $i_{rst,h}(t)$ on the rotating frame rotating at rotor asymmetry fault frequency	A	ω_n	*n*-harmonic angular frequency	rad/s
$i_{xr1fsup}(t)$	Current phasor $i_{rst,h}(t)$ on the rotating frame rotating at supply frequency	A			

8 References

[1] A. Bellini; F. Filippetti; C. Tassoni; G-A. Capolino, Advances in diagnostic techniques for induction machines. *IEEE Trans. Ind. Electron. 2008, Vol. 55(12), pp. 4109–4126.*

[2] V. Ghorbanian; G. Joksimović; J. Faiz, Fault Diagnosis of Induction Motors; *Institution of Engineering & Technology, 2017.*

[3] H.A. Toliyat; S. Nandi; S. Choi; H. Meshgin-Kelk, Electric Machines: Modeling, Condition Monitoring, and Fault Diagnosis; CRC press, 2002.

[4] P. Panagiotou, Reliable Detection of Rotor Electrical Faults in Induction Motors Using Frequency Extraction of Stator Current and Stray Magnetic Flux Signals, Ph.D. dissertation, Coventry University, 2020.

[5] J. Bonet-Jara; D. Morinigo-Sotelo; O. Duque-Perez; L. Serrano-Iribarnegaray; J. Pons-Llinares, End-ring wear in deep-well submersible motor pumps. *IEEE Trans. Ind. Appl. 2022, Vol. 58(4), pp. 4522–4531.*

[6] S.B. Lee, et al., Identification of false rotor fault indications produced by online MCSA for medium-voltage induction machines. *IEEE Trans. Ind. Appl. 2016, Vol. 52(1), pp. 729–739.*

[7] I.D. Lomax, Assessment of Induction Motor Cage Fatigue Life. *In Proceedings of 1991 Fifth International Conference on Electrical Machines and Drives, London, UK, 11-13 September 1991.*

[8] D.G. Dorrell; L. Frosini; M. Bottani; G. Galbiati; M-F. Hsieh, Analysis of Axial Voltages and Inter-Bar Currents in Cast Copper Cage Rotors During DC Current Injection as an Aid to Identify Casting Faults. *In Proceedings of 2009 35th Annual Conference of IEEE Industrial Electronics, Porto, Portugal, 03-05 November 2009.*

[9] F. Filippetti; G. Franceschini; C. Tassoni; P. Vas, AI techniques in induction machines diagnosis including the speed ripple effect. *IEEE Trans. Ind. Appl. 1998, Vol. 34(1), pp. 98–108.*

[10] M. Riera-Guasp; J.A. Antonino-Daviu; G.-A. Capolino, Advances in electrical machine, power electronic, and drive condition monitoring and fault detection: State of the art. *IEEE Trans. Ind. Electron. 2015, Vol. 62(3), pp. 1746–1759.*

[11] A. Bellini; F. Filippetti; G. Franceschini; C. Tassoni; G.B. Kliman, Quantitative evaluation of induction motor broken bars by means of electrical signature analysis. *IEEE Trans. Ind. Appl. 2001, Vol. 37, p.p. 1248–1255.*

[12] L. Frosini, Novel diagnostic techniques for rotating electrical machines—A review. *Energies 2020, Vol. 13(19), 5066.*

[13] M.E.E.-D. Atta; D.K. Ibrahim; M.I. Gilany, Broken bar fault detection and diagnosis techniques for induction motors and drives: state of the art. *IEEE Access 2022, Vol. 10, pp. 88504-88526.*

[14] O. AlShorman; M. Irfan; R. B. Abdelrahman; M. Masadeh; A. Alshorman; M. A. Sheikh; N. Saad; S. Rahman, Advancements in condition monitoring and fault diagnosis of rotating machinery: A comprehensive review of image-based intelligent techniques for induction motors, *Engineering Applications of Artificial Intelligence*, Volume 130, 2024.

[15] K.N. Gyftakis; P.A. Panagiotou; S.B. Lee, Generation of mechanical frequency related harmonics in the stray flux spectra of induction motors suffering from rotor electrical faults. *IEEE Trans. Ind. Appl. 2020, Vol. 56(5), pp. 4796–4803.*
[16] P.A. Panagiotou; I. Arvanitakis; N. Lophitis; J.A. Antonino-Daviu; K.N. Gyftakis, A new approach for broken rotor bar detection in induction motors using frequency extraction in stray flux signals. *IEEE Trans. Ind. Appl. 2019, Vol. 55, pp. 3501–3511.*
[17] J.E. Garcia-Bracamonte; J.M. Ramirez-Cortes; J. de Jesus Rangel-Magdaleno; P. Gomez-Gil; H. Peregrina-Barreto; V. Alarcon-Aquino, An approach on MCSA-based fault detection using independent component analysis and neural networks. *IEEE Trans. Instrum. Meas. 2019, Vol. 68(5), pp. 1353–1361.*
[18] M. Drakaki; Y.L. Karnavas; A.D. Karlis; I.D. Chasiotis; P. Tzionas, Study on fault diagnosis of broken rotor bars in squirrel cage induction motors: A multi-agent system approach using intelligent classifiers. *IET Electr. Power Appl. 2020, Vol. 14(2), pp. 245–255.*
[19] T.-T. Vo; M.-K. Liu; M.-Q. Tran, Harnessing attention mechanisms in a comprehensive deep learning approach for induction motor fault diagnosis using raw electrical signals, *Engineering Applications of Artificial Intelligence*, Volume 129, 2024.
[20] A. Abdulkareem; T. Anyim; O, Popoola; J. Abubakar; A. Ayoade, Prediction of induction motor faults using machine learning, *Heliyon*, Volume 11, Issue 1, 2025.
[21] C. Orellana; L. Ortiz; A. Aguila; M. Garcia; M. Ruiz, Hybrid algorithm for fault detection in three-phase motors using Principal Component Analysis, *e-Prime - Advances in Electrical Engineering, Electronics and Energy*, 2025.
[22] F. J. Basha; K. Somasundaram, Rotor Asymmetry Detection in Wound Rotor Induction Motor Using Kalman Filter Variants and Investigations on Their Robustness: An Experimental Implementation. *Machines*, 2023, 11, 910.
[23] R. Puche-Panadero; J. Martinez-Roman; A. Sapena-Bano; J. Burriel-Valencia; M. Pineda-Sanchez; J. Perez-Cruz; M. Riera-Guasp, New method for spectral leakage reduction in the FFT of stator currents: Application to the diagnosis of bar breakages in cage motors working at very low slip. *IEEE Trans. Instrum. Meas. 2021, Vol. 70, pp. 1–11.*
[24] G.R. Bossio; C.H.D. Angelo; J.M. Bossio; C.M. Pezzani; G.O. Garcia, Separating broken rotor bars and load oscillations on IM fault diagnosis through the instantaneous active and reactive currents. *IEEE Trans. Ind. Electron. 2009, Vol. 56(11), pp. 4571–4580.*
[25] M. Meira, C. Ruschetti; C. Verucchi; G. Bossio; J. Bossio, Diagnosis of induction motor faults using the full spectrum of direct and quadrature currents. *In Proc. 19th Workshop Inf. Process. Control (RPIC), SAN JUAN, Argentina, Nov. 2021, pp. 1–6.*
[26] R. Bazghandi; M.H. Marzebali; V. Abolghasemi, Asymmetrical Fault Detection in Induction Motors Through Elimination of Load Torque Oscillations Effects in the Slight Speed Variations and Steady-State Conditions, *IEEE Journal of Emerging and Selected Topics in Industrial Electronics*, vol. 4, no. 3, pp. 725-733, July 2023
[27] S.M.A. Cruz; A.J.M. Cardoso, Rotor cage fault diagnosis in three-phase induction motors by extended Park's vector approach. *Electric Mach. Power Syst. 2000, Vol. 28, pp. 289–299.*
[28] C.M. Pezzani; P.D. Donolo; A.M. Castellino; G.R. Bossio; C.H. De Angelo, A New Approach to the Park's Vector for Broken Bars and Load Oscillation Diagnosis on IM. *In Proceedings of the 2010 IEEE International Conference on Industrial Technology, Via del Mar, Chile, 14–17 March 2010.*
[29] K. Bacha; S.B. Salem; A. Chaari, An improved combination of Hilbert and Park transforms for fault detection and identification in three-phase induction motors. *Int. J. Electr. Power Energy Syst. 2012, Vol. 43, pp. 1006–1016.*
[30] K.N. Gyftakis; A.J.M. Cardoso; J.A. Antonino-Daviu, Introducing the Filtered Park's and Filtered Extended Park's Vector Approach to detect broken rotor bars in induction motors independently from the rotor slots number. *Mech. Syst. Signal Proc. 2017, Vol. 93, pp. 30–50*.
[31] R.R. Kumar; L.O. Waisale; J.L. Tamata; A. Tortella; S.H. Kia; M. Andriollo, Advanced Fault Detection and Severity Analysis of Broken Rotor Bars in Induction Motors: Comparative Classification and Feature Study Using Dimensionality Reduction Techniques. *Machines* 2024, 12, 890.
[32] W. Purbowaskito; C.-y. Lan; K. Fuh, Introducing Model-Based Residual Spectrum Analysis for a Practical Improvement in Induction Motors Fault Diagnosis, *IEEE Transactions on Energy Conversion*, vol. 39, no. 3, pp. 1958-1971, Sept. 2024
[33] T. Bedida; S. Makhloufi; Y. Bekakra; M. Kermadi; N. Bessous; R. Kechida; D. Taibi, Predictive torque control of induction motor for rotor bar faults diagnosis, *Energy Reports*, Volume 11, 2024, pp. 4940-4956,
[34] W. Deleroi, Squirrel Cage Motor with Broken Bar in the Rotor – Physical Phenomena and their Experimental Assessment. *In Proceedings of Int. Conf. Electrical Machines, Budapest, Hungary, 5-9 September 1982.*
[35] Modern Electrical Drives, H. Bulent Ertan, M. Yildirim Uctug, Ron Colyer, Alfio Consoli, Springer Link, 2000.
[36] Modern Power Electronic and AC Drives, 1st ed.; B. K. Bose, Prentice Hall: Upper Saddle River, USA, 2001.
[37] Determining Electric Motor Load and Efficiency, Program of the U.S. Department of Energy (https://www.energy.gov/eere/amo/articles/determining-electric-motor-load-and-efficiency) Last accessed 26/02/2025.